High-throughput volatile organic compounds removal in a sandwich-type honeycomb catalyst system combined with plasma

Van Toan Nguyen [a], Duy Khoe Dinh [b], Young Sun Mok [a,*], Kyeong Hwan Yoon [a], Van Duong Dao [c], Md. Mokter Hossain [a], Shirjana Saud [a], Teke Sosiawati [a]

[a] *Department of Chemical and Biological Engineering, Jeju National University, Jeju 63243, Republic of Korea*
[b] *Department of Industrial Plasma Engineering, Korea Institute of Machinery and Materials, Daejeon 34103, Republic of Korea*
[c] *Faculty of Biotechnology, Chemistry and Environmental Engineering, Phenikaa University, Hanoi 10000, Viet Nam*

ARTICLE INFO

ABSTRACT

This paper reports on the ethyl acetate (EA) removal over a honeycomb catalyst using an experimental design methodology. A mathematical model based on the response surface methodology is developed to evaluate the effect of parameters such as specific input energy (SIE), humidity, and EA concentration on the response variables (i.e., removal and energy efficiency). A set of experiments based on a statistical three-level full-factorial design of the experimental method were performed to collect the removal data. The model ($R_1^2 = 0.9858$ and $R_2^2 = 0.9305$ for removal and energy efficiency, respectively) indicates a satisfactory correlation between the experimental and predicted values. The analysis results using the model show that SIE is the principal parameter affecting the EA removal. Besides, verification of the experimental results indicates that the EA removal of 90.93% and the energy efficiency of 2.91 $g.kWh^{-1}$ at 235 J L^{-1}, 1.5%, and 30.3 ppm were achieved under optimal conditions.

1. Introduction

Ethyl acetate (EA) is a typical gaseous volatile organic compound (VOCs), which is chosen as a model of environmental pollution since it is manufactured on a large scale for use as a solvent in industry [1–3]. Furthermore, it is toxic gas; a low concentration of EA can cause nausea, dizziness, and even cancer [1,4]. Considerable efforts have been devoted to reducing the levels of VOCs by using absorption and adsorption [5,6], thermal incineration with or without catalysts [7–9], biological treatment [10], nonthermal plasma (NTP), and nonthermal plasma catalysis [1,11]. However, these conventional methods are inefficient to remove low concentrations of VOCs in high volume waste gas streams because of the high energy cost, slow reaction rate, high investment and operational cost, high-temperature operational requirements. For example, the drawbacks of the adsorption and absorption method are post-treatment/reactivating and disposal of used adsorbents, which may lead to an increase in the overall cost. Thermal incineration and catalytic oxidation require large amounts of energy for heating the high volume gas flow to clean only a low concentration of VOC. Although catalysis is featured as a selective process, most traditional catalysts are activated at

high temperatures (300–600 ℃); at room temperature, they function similarly to adsorbents. The catalytic deactivation represents a serious problem for this technology [3,9]. The disadvantage of the biological treatment method is the slow biological oxidation of less water-soluble and less biodegradable VOCs, the system is very large and non-competitive [10,12]. In recent years, NTP has been considered a promising method for the removal of a wide range of low concentration VOCs under ambient conditions. The high-energy electrons and reactive species produced in the plasma zone are highly efficient at breaking most chemical bonds or initiating a series of chemical reactions, resulting in the degradation of VOC molecules [13,14]. However, a disadvantage of NTP technology is incomplete oxidation that leads to the formation of unwanted byproducts [1]. Therefore, a combination of heterogeneous catalysis with NTP is an effective approach for the high throughput removal of low concentrations of pollutions at low temperatures [1,15]. This method is high economic value (low energy cost), reduced secondary pollutants generation, and operated at room temperature because of the combination of advantages of both the catalyst and plasma [16–18]. The catalyst can enhance plasma formation, micro-discharge generation, and the distribution of active species. On

the other hand, plasma can improve the properties of the catalyst, regenerate the activity ability of the catalyst, and generate more active species (atoms, ions, electrons, free radicals, photons, etc.) [19,20]. The plasma catalyst reactor configurations commonly used for pollution removal are dielectric barrier discharge (DBD) [1,21,22] and corona discharge reactors [19,23]. The DBD reactor configuration is reportedly capable of removing VOCs with high efficiency and generating steady-state plasma [1,21,24]. Unfortunately, the short discharge gap to within a few millimeters and the large pressure drop of the gas passing through the pellets or powder catalyst layer of the packed bed in the DBD reactor have significantly limited its practical applicability [19,25]. In comparison, the corona discharge reactor configuration has two parallel perforated disk electrodes [26,27], which results in a longer plasma discharge gap up to several centimeters. Therefore, this reactor is more suitable for combination with a commercial-scale honeycomb catalyst, which is widely used because of its unique features such as its larger surface area, uniform distribution of gas flow, mass transfer, thermal stability, and good mechanical strength [8,28,29]. Herein, a real-scale sandwich-type honeycomb catalyst coated with a layer of γ-alumina (γ-Al_2O_3) powder to form the support for a palladium (Pd) catalyst was used to study the removal of low concentrations of EA from the air.

Most previous studies focused on investigating and optimizing the removal efficiency of VOCs by using plasma catalysis systems via experimental approaches [1,2,26]. However, this traditional method requires many experiments to optimize the process, which is time-consuming, expensive, and labor-intensive. Furthermore, these studies mainly focused on the independent influence of each of the individual process parameters [15]. The interactions between different independent variables that affect the observed responses would have unexplained variability owing to extraneous factors and would be considered inadequate to provide practical guidelines for industrial applications. Recently, a statistical model based on a design of experiments (DoE) using response surface methodology (RSM) has attracted attention to investigate and optimize various complex processes. The model is suitable to explore the interaction effects of multiple independent variables and their influence on the responses variables [30]. RSM is a valuable kind of mathematical, theoretical, and statistical technique, commonly used to model, analyze, and optimize processes in engineering problems [30,31]. RSM can provide information on the nonlinear correlation between the input parameters and the output results. Nonetheless, up to now, the application of RSM in the optimization of plasma catalytic reactors has scarcely been investigated.

The present work is mostly concerned with the high throughput removal of EA using a real-scale honeycomb catalyst coupled with NTP at atmospheric pressure. The effects of various input parameters (i.e., SIE, water vapor, and initial EA concentrations), and their mutual influence on the response variables (i.e., removal efficiency and energy efficiency) of EA removal in a plasma and catalyst reactor were also investigated using RSM. The experimental data were analyzed through multiple regressions to fit quadratic polynomial equations for the independent variables. An analysis of variance (ANOVA) was performed to check the significant difference and the interaction between these variables. The operating conditions for EA removal in the plasma-catalyst reactor were optimized to achieve the maximum EA removal efficiency. In addition, the characteristics of the catalyst were analyzed to gain insight into the roles of the catalyst in the oxidation reaction.

2. Materials and methods

2.1. Catalyst preparation and characterization

2.1.1. Synthesis of the catalysts

A real-scale sandwich-type honeycomb monolith catalyst was used in this work (50 × ϕ 93 mm, 300 cpsi, the dimensions of each cell being 1 × 1 mm, 0.33 mm average wall thickness Ceracomb Co., Korea). The
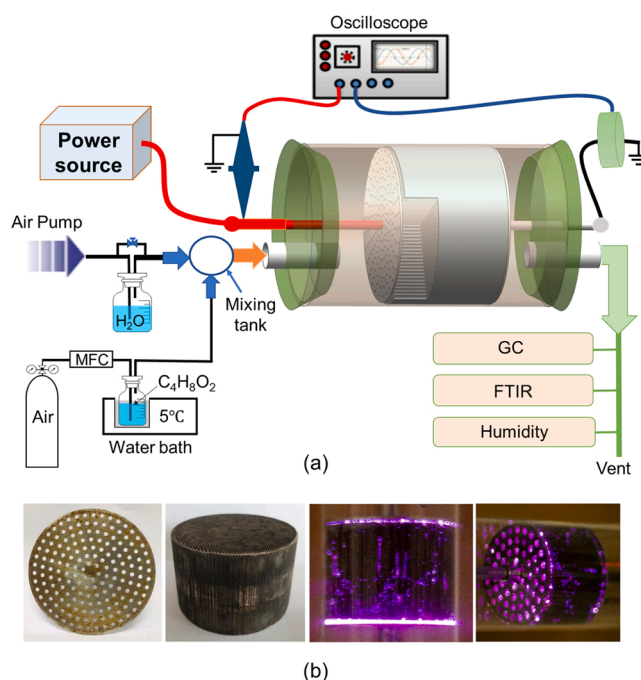

Fig. 1. (a) Schematic diagram of the experimental setup, (b) the images of the electrode, sandwich-type honeycomb catalyst, and discharge plasma of the reactor.

honeycomb monolith was coated with commercial γ-Al_2O_3 (powder, Alfa Aesar. Co., Ltd.) powder by the wash coating method and formed support for Pd, which was deposited by the incipient wetness impregnation method (Fig. 2). A detailed description of the catalyst preparation can be found in the previous study [26]. Briefly, the bare monolith was dipped into a slurry of alumina (alumina powder: SiO_2: ethanol: deionized water in a mass ratio of 1: 0.5: 4: 4). After the coated layer was uniform and the expected loading amount was reached, the samples were dried overnight at 110 °C, consequently calcined at 550 °C for 6 h in a tube furnace equipped with a proportional-integral-derivative (PID) controller (DTF-50300, Daeheung Science Co., Korea). The palladium (Pd) (2.0 wt% of powder amount coating on the honeycomb) was supported on the γ-Al_2O_3/honeycomb by the incipient wetness impregnation method. An appropriate amount of palladium nitrate Pd $(NO_3)_2 \cdot 2H_2O$ was added to deionized water and stirred at room temperature for 30 min before being completely dispersed in an ultrasonic bath to obtain a liquid with 2.0 wt% Pd. The γ-Al_2O_3/honeycomb was immersed in the aqueous solution of Pd$(NO_3)_2 \cdot 2H_2O$. Then the catalysts were dried at 110 °C overnight and calcined at 550 °C for 6 h in a tube furnace. This procedure was repeated until the entire solution had been used to impregnate the γ-Al_2O_3/honeycomb-structure monolith. The Pd loading is controlled at 2.0 wt%, (Pd$_{0.02}$/γ-Al_2O_3/honeycomb catalyst).

2.1.2. Catalyst characterizations

The structure and phase purity of the synthesized catalysts were confirmed by scanning electron microscopy (SEM) (MIRA3, TESCAN instrument, Czech Republic). X-ray photoelectron spectroscopy (XPS) analysis was conducted using an Axis-Supra instrument equipped with an automated monochromatic X-ray source: Al (1486.7 eV)/Ag (eV). The XPS results were used to identify the relative concentrations of metal ions and oxygen species, which were calculated based on the areas of the corresponding peaks. The metal contents of the honeycomb catalyst were analyzed by using an inductively coupled plasma optical emission spectrophotometer (ICP-OES, Perkin Elmer OPTIMA 8300, USA). The powder X-ray diffraction (XRD) patterns were analyzed by a PANalytical EMPYREAN instrument using monochromatic Cu-Kα radiation. The data were collected in the range of 5–90 °C (2θ) at a scanning

Table 1
Experimental factors and levels of the independent variables.

Independent variables	Symbols		Levels			Step change value (ΔX_i)
	Uncodified	Codified	Low (−1)	Middle (0)	High (+1)	
Specific input energy (*SIE*)	X_1	x_1	80	160	240	80
Water vapor (%)	X_2	x_2	1.5	2.1	2.7	0.6
Initial concentration (*ppm*)	X_3	x_3	30	60	90	30

rate of 2° (2θ)/min. XRD analysis was carried out to determine the structure and crystallinity of the catalysts.

2.2. Description of the experimental setup

Fig. 1(a) shows a schematic diagram of the experimental system, which consists of the reaction gas supply, a honeycomb corona plasma reactor, a high voltage power supply, and gas analytical instrumentation. The reaction gas containing EA and a certain amount of water vapor was introduced into the reactor. The initial EA concentration was generated by passing an air flux through a bubbler containing pure EA liquid (99.9%, DEAJUNG) kept in a water bath (5 °C). The airflow rate was monitored by a mass flow controller (MFC, Model 1179A, MKS Instruments, Inc., Wilmington, MA, USA). The relative humidity of the gas was controlled by adjusting the gas flow through the water bottle at room temperature. The main airflow was produced by an air pump and the flow rate was fixed at GHSV of 10,000 h^{-1}. A gas chromatograph (GC, Bruker 450-GC, USA) with a flame ionization detector (FID) was used to analyze the EA to determine the concentration. The byproducts and CO_2 concentration were quantified using a Fourier transform infrared spectrophotometer (FTIR-7600, Lambda Scientific, Australia) with a 21 cm long gas cell. The organic byproducts after the reaction were examined using gas chromatography and mass spectrometry (GC-MS, IQS QD300, Thermo Fisher). The EA conversion (η (%)) and the selectivity towards CO_2 were calculated as follows.

$$\eta \quad (\%) = \frac{C_{C_4H_8O_2}^{in} - C_{C_4H_8O_2}^{Out}}{C_{C_4H_8O_2}^{in}} \times 100 \quad \% \tag{1}$$

$$S_{CO_2} = \frac{C_{CO_2}}{4 \times (C_{C_4H_8O_2}^{in} - C_{C_4H_8O_2}^{out})} \times 100\% \tag{2}$$

where $C_{C_4H_8O_2}^{in}$ (ppm) and $C_{C_4H_8O_2}^{out}$ (ppm) are the concentrations of EA in the inlet and outlet of the reactor, respectively. C_{CO_2} is the concentration of CO_2 after the oxidation reaction.

The reactor consists of a quartz cylinder configuration, a sandwich-type honeycomb catalyst (ϕ93 × 50 mm), and two stainless-steel perforated disks (ϕ93 × 2 mm) (Fig. 1). The honeycomb catalyst is placed between two electrodes, allowing the plasma to directly activate the catalyst. The discharge gap was 52 mm, whereas the distance from the outer electrode to the honeycomb surface was 2 mm. AC high-voltage power with a frequency of 400 Hz is employed to create the corona discharge inside the honeycomb catalyst. A high-voltage probe (P6015A, Tektronix, USA, 1000:1) was used to measure the applied voltage of the discharge, while the current was measured by using a current probe (Model 2100, Pearson, USA). All the electrical data were recorded by a digital oscilloscope (TBS1064, Tektronix, USA). The average discharge power (P) and specific input energy (SIE) were calculated as follows:

$$P(W) \quad = \frac{1}{T} \int_0^T V(t)I(t)dt \tag{3}$$

Table 2
Experimental design matrix and observed values based on central composite design (CCD) used in this study.

Run order	Codes values (X)			Experimental data		Predicted value	
				Responses (Y)			
	X_1	X_2	X_3	Y_1 (%)	Y_2 (g/kWh)	Y'_1 (%)	Y'_2 (g/kWh)
1	240	2.1	60	86.60	1.92	87.33	1.87
2	240	2.7	30	89.60	0.97	88.45	1.32
3	80	2.7	30	57.78	1.92	55.21	1.76
4	160	2.7	60	70.58	2.24	70.08	2.12
5	80	1.5	30	63.15	2.16	63.61	2.5
6	160	2.1	60	75.79	2.46	75.44	2.45
7	240	1.5	30	92.11	1.04	91.23	0.91
8	160	2.1	60	75.79	2.46	75.44	2.45
9	160	2.1	60	75.79	2.46	75.44	2.45
10	240	2.7	90	79.10	2.56	76.38	2.42
11	160	2.1	60	75.79	2.46	75.44	2.45
12	80	2.1	60	51.29	3.40	51.59	3.34
13	160	2.1	30	81.80	1.36	82.23	1.47
14	160	2.1	90	65.01	3.24	65.62	3.33
15	240	1.5	90	82.37	2.73	84.68	3.02
16	80	2.7	90	25.32	2.52	28.24	2.68
17	160	1.5	60	78.89	2.62	80.42	2.78
18	160	2.1	60	75.79	2.46	75.44	2.45
19	160	2.1	60	75.79	2.46	75.44	2.45
20	80	1.5	90	51.57	5.13	48.45	4.91

$$SIE(J/L) \quad = \frac{P(W)}{Q(\frac{L}{min})} \times \quad 60(\frac{s}{min}) \tag{4}$$

The energy efficiency (EE) was calculated using Eq. (5) [22].

$$EE(g/kWh) = \frac{3.6 \times 10^6 \times M_{ethyl\ acetate} \times \eta \times C_{in} \times F}{P \times V_m} \tag{5}$$

where $M_{ethyl\ acetate}$ is the formula mass of EA (g/mol); F is the total flow rate (L/min); P is the discharge power (W); V_m is the gas molar volume; 3.6 is a factor to obtain EE in g/kWh units.

All experiments were carried out at room temperature and atmospheric pressure.

2.3. Response surface methodology (RSM)

In this work, a mathematical regression method based on RSM was used to establish the relationship between the independent variables, including the specific input energy (SIE) (X_1), humidity (X_2), and initial concentration (X_3) and response variables, such as the removal efficiency (Y_1) and energy efficiency (Y_2). The RSM design along with coded and uncoded levels is shown in Table 1. The central composite design (CCD) (three-factor and three-level) and quadratic model were used to characterize the interaction between the process variables and the response variables [30,31]. Based on Table 1, the CCD was applied to a total of 20 experiments, including six axial points, eight fractional points, and the central points (with 6 repeats to enhance the uniform precision) were taken according to the CCD, summarized in Table 2.
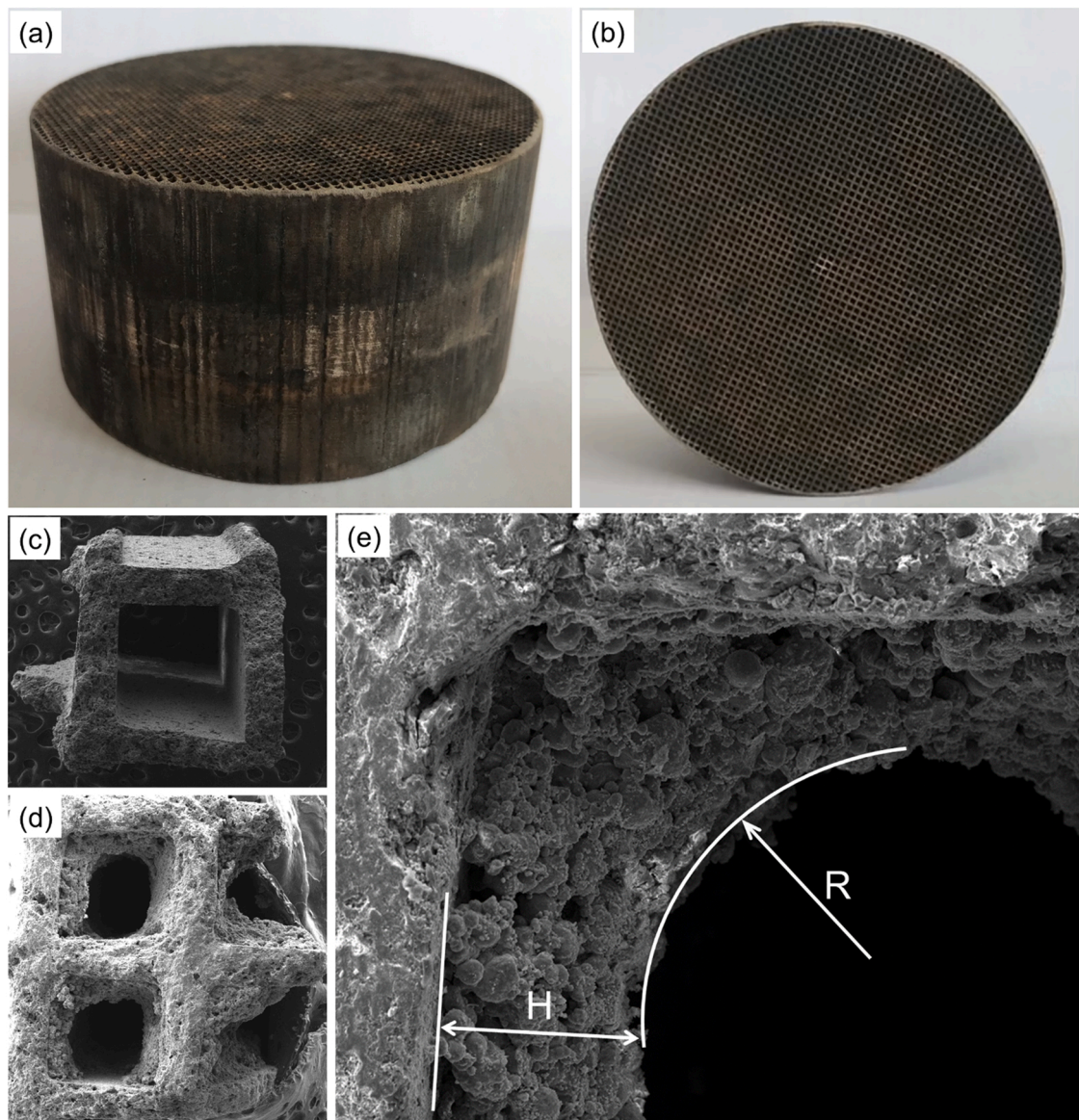
Fig. 2. (a-b) Images (side and top view) of the sandwich-type honeycomb monolith catalysts used in this work, (c) SEM image of the channels of the bare honeycomb monolith, (d-e) SEM images of the thickness of the coating in the corners and against the walls of the channels of the coated honeycomb monolith.

The variables are coded according to the following Eq. (6).

$$x_i = \left((X_i - \overline{X_i}) / \Delta X_i \right) \qquad (6)$$

Here x_i represents the coded independent variable, X_i indicates the real value of the independent variable, $\overline{X_i}$ is the real value of an independent variable at the center point, and ΔX_i is the step-change. The specific codes for the independent variables are shown in Eqs. (7)–(9).

$$x_1 = (X_1 - 160)/80 \qquad (7)$$

$$x_2 = (X_2 - 2.1)/0.6 \qquad (8)$$

$$x_3 = (X_3 - 60)/30 \qquad (9)$$

The effect of the independent variables on response variables, contour plots, and response surface plots was created by using Design-Expert software 12 (DoE, Stat-Ease Inc., USA). The influences of the various operating parameters on the EA removal efficiency are accurately investigated using Eq. (10):

$$Y = \beta_0 + \sum_{i=1}^{k} \beta_i x_i + \sum_{i=1}^{k} \beta_{ii} x_i^2 + \sum_{i=1}^{k-1} \sum_{j=i+1}^{k} \beta_{ij} x_i x_j \qquad (10)$$

where the responses (Y) are predicted or output variables; $x_i, x_j, \ldots, x_k$ are input variables; $x_i^2, x_j^2, .., x_k^2$ are the square effects; $x_i x_j, x_i x_k, \ldots, x_j x_k$ are the interaction effects; and $\beta_0, \beta_i, \beta_{ij}$ are estimated coefficients [31].

3. Results and discussion

3.1. Physicochemical properties of the catalysts

Fig. 2 shows images of the sandwich-type honeycomb catalysts used in this work. The difference between channels of the bare monolith and channels of the monolith with the coating layer was obtained. The thickness of the coating layer in the corners and on the walls of the monolith channel (Fig. 2(d and e)), is uniformly controlled along the entire channel length. The coating on the channel walls and in the corners of the monolith structure enlarges the specific surface area that is available to support the metallic active components, indicating clear
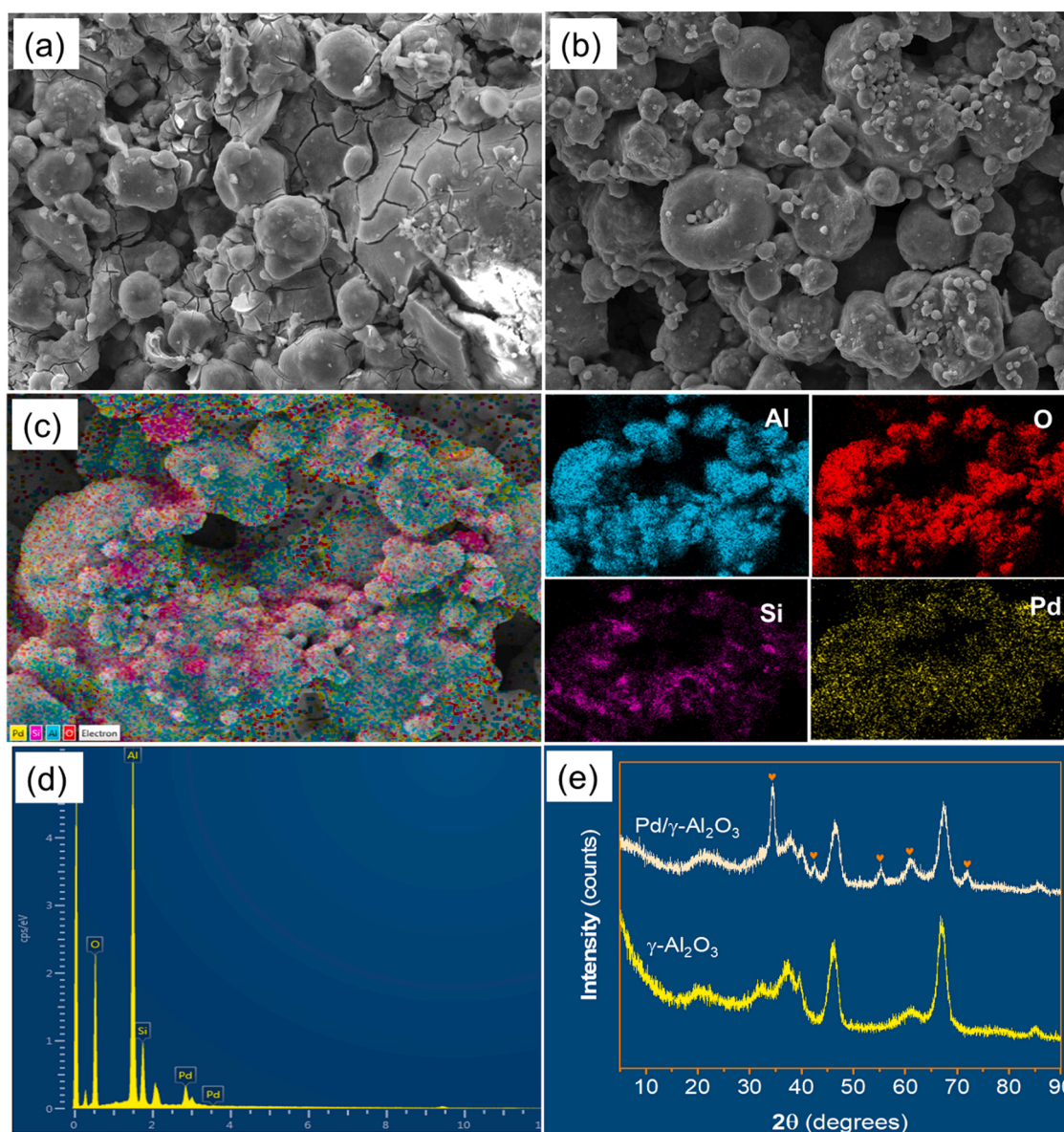
Fig. 3. Structural properties of the catalyst used in this work; SEM images of (a) γ-Al_2O_3/honeycomb monolith, and (b) Pd/γ-Al_2O_3/honeycomb monolith; (c-d) EDS elemental mapping images for a selected area of the Pd$_{.02}$/γ-Al_2O_3/honeycomb monolith; and (e) X-ray diffraction patterns of γ-Al_2O_3 and Pd/γ-Al_2O_3 catalyst layers coated onto the honeycomb monolith.

advantages over the conventional ceramic-supported catalysts. In addition, the coating layer with the catalyst plays an important role in plasma-catalytic chemical reactions, improves the catalytic performance, and creates more catalyst active sites [13]. The results of the ICP-OES analysis show that the metal component of the honeycomb catalyst consisted of 2.0 wt% Pd.

Fig. 3(a and b) shows SEM images of the γ-Al_2O_3 and Pd/γ-Al_2O_3 coatings on the honeycomb monolith. This visualization points out that both the alumina oxide and palladium completely covered the surface of the bare monolith. However, the SEM image (Fig. 3(a)) shows the appearance of many cracks on the surface of the alumina coating, resulting in poor stability of the coating layer. Fig. 3(b) indicates that PdO particles are well dispersed in the γ-Al_2O_3 grains. An interesting point here is that the cracks seem to have completely disappeared once the Pd was deposited. It can be inferred that the cracks were filled with PdO particles, suggesting a significant enhancement of the coating layer. Indeed, the stability of the catalyst coating layer on the monolith is one of the most important properties determining their efficiency in

practical applications. The Pd coating significantly changes the physicochemical characteristics of the catalysts and catalytic activity [32,33]. The dispersion of Pd on the alumina surface was reconfirmed through energy-dispersive X-ray spectroscopy (EDS) elemental mapping images and the elemental composition of a selected area of the coating layer surface (Fig. 3(c and d)). Al, Si, O, and Pd coexist on the catalyst surface and act as catalytically active sites that are well distributed over the surface. Fig. 3(e) shows the XRD patterns of the γ-Al_2O_3 and Pd/γ-Al_2O_3 catalysts layer coating on the honeycomb monolith. A noteworthy result of the analysis is that the crystalline phase of PdO exhibited well-resolved peaks with a sharp peak positioned at $2\theta = 34.3°$, $42.1°$, $55.3°$, $61.5°$, and $71.6°$ for the respective crystal planes (101), (110), (112), (200) and (202) of palladium oxide species [34]. This observation also confirmed that PdO particles crystallize and are well dispersed on the support surface of the Pd/γ-Al_2O_3 catalyst.

To gain deeper insight into the surface composition, electronic state of the catalyst, and the interaction between the support and active metal component, XPS measurements were carried out. The specific elemental
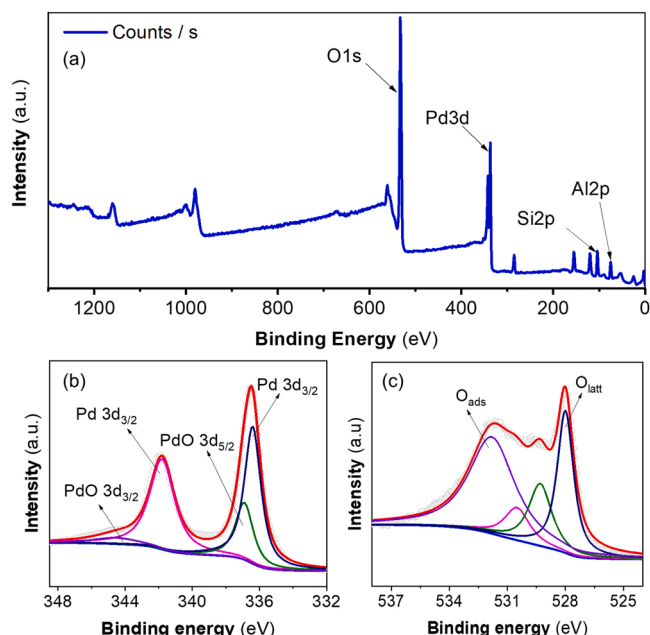
Fig. 4. XPS spectra of the Pd/γ-Al₂O₃/honeycomb monolith catalyst.

XPS results of the catalyst are displayed in Fig. 4. It was found that there are two distinct peaks at 336.5 and 341.8 eV which were assigned to Pd $3d_{3/2}$ and Pd $3d_{5/2}$, respectively [35]. The binding energies of the Pd $3d_{3/2}$ peak for the catalyst were found to have the highest intensity. The binding energies of the Pd $3d_{3/2}$ peak are conclusive in terms of the presence of PdO species on the catalyst surface [36]. The metallic Pd in these bimetallic particles was oxidized into PdO clusters under high-temperature conditions (calcined at 550 °C) [33,35,36]. The higher chemical shifts of Pd $3d_{5/2}$ and Pd $3d_{3/2}$, as indicated in Fig. 4(b), reconfirm the strong interaction between the support and PdO species. This finding is in good agreement with EDS elemental mapping images and XRD patterns (Fig. 3), where the well-dispersed PdO particles are supported on the surface of the catalyst. The presence of PdO on the catalyst surface is crucial for the oxidation of VOCs [36,37]. Apart from this, the asymmetric O1s peaks with the two-band structure are observed in Fig. 4(c). The peak at around 532.2 eV was identified as the formation of surface adsorbed oxygen (O_{ads}), whereas those at 526.5 eV are assigned to the generation of lattice oxygen (O_{lat}) [38]. The ratio of $O_{ads}/(O_{lat} + O_{ads})$ could also be considered as an indication of the amount of oxygen vacancies [38,39]. Oxygen vacancies act as the adsorption-desorption centers for O radicals [40,41]. Higher content of surface-adsorbed oxygen (O_{ads}) derived from oxygen vacancies promotes higher catalytic activity for VOC degradation [38,42]. In addition, low binding energy was detected in Al2p (74.38 eV) and Si2p (103.4 eV) with Pd doping (Fig. 4(a)). The co-existence of more Pd^{2+} species and a higher proportion of lattice oxygen on the surface of catalysts was responsible for the high catalytic activity for EA oxidation.

3.2. Ethyl acetate removal efficiency

Fig. 5(a) shows the time-based variations in the EA concentration in the different reactors. The obtained result indicates that without plasma, EA is only absorbed on the γ-Al₂O₃ and Pd/γ-Al₂O₃ catalyst coatings on the honeycomb monolith and that these catalysts were not activated to convert EA at room temperature. As observed, initially the EA was almost completely adsorbed on the catalyst, after which the concentration of EA gradually increased, and reached the initial concentration in 60 min. The uptake capabilities of the Pd/γ-Al₂O₃ catalyst were higher than those of the γ-Al₂O₃ catalyst. More effective adsorption subsequently prolongs the retention time of pollutants in the reaction zone, leading to increases in the probability of collision between pollutant molecules and radicals or active species, resulting in a shift towards total oxidation [43,44]. An interesting observation here was that when the plasma was used, the EA was first adsorbed and decomposed in 45 min, and then the EA removal efficiency over the γ-Al₂O₃ and Pd/γ-Al₂O₃ catalysts was maintained at approximately 54.2% and 83.5%, respectively. Evidently, the combination of the plasma with the catalysts strongly enhanced the EA removal efficiency at atmospheric pressure [2,40]. It is well accepted that energetic electrons and reactive species are generated in the plasma zone, which is beneficial for the initiation of plasma-induced reactions and consequently oxidizes EA and its intermediates to the final products [1,4]. In addition, the Pd/γ-Al₂O₃-honeycomb catalyst, which has a high catalytic activity owing to its supported palladium (Pd), further improved the adsorption capacity and catalyst activity [32,45]. Note that the catalysts were calcinated again at 550 °C for 6 h to remove all the adsorbed substances before the plasma was used in these experiments.

In this work, the main gaseous products after the plasma catalytic EA oxidation process were CO_2 and H_2O. A small amount of inorganic byproducts and organic byproducts such as O_3, acetone, etc. was detected. Fig. 5(b) indicates the CO_2 selectivity of various processes of the honeycomb system. As an observation, the CO_2 selectivity of the catalyst process at room temperature is zero, which indicates the EA is not oxidized. Notably, the CO_2 selectivity is greatly enhanced by the plasma inside the catalyst. This phenomenon may be ascribed to the high-energy electrons and reactive species generated in the plasma zone
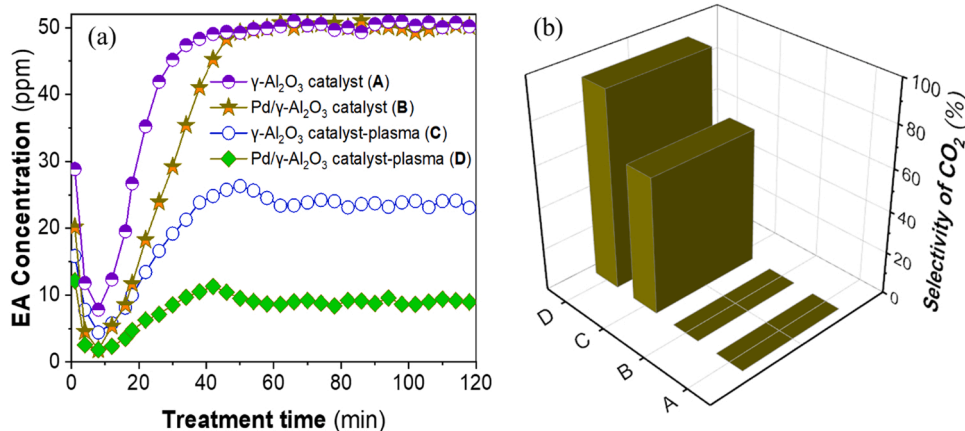

Fig. 5. (a) EA removal efficiency over γ-Al₂O₃/honeycomb and Pd/γ-Al₂O₃/honeycomb catalysts with and without plasma; (b) CO₂ selectivity (GHSV: 10.000 h⁻¹, water vapor: 2.1%, EA inlet: 50 ppm, SIE: 190 J/L).
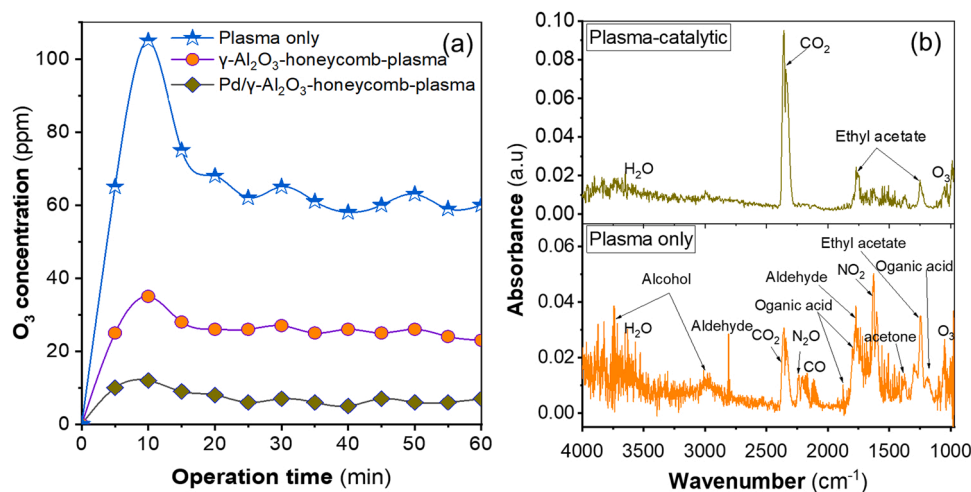
Fig. 6. Byproducts obtained from the plasma and plasma catalysis process (a) temporal variations in the O_3 concentration; (b) FTIR spectrum of the effluent gases (500 ppm EA, dry air, SIE: 190 J/L).

that destroy the chemical bonds of EA molecules in both the gas-phase reaction and reactions on the catalyst surface. Fig. 6(a) shows the temporal variations in the O_3 concentration in the effluent stream over plasma alone, and for plasma in combination with the catalysts (i.e., γ-Al$_2$O$_3$-honeycomb and Pd/γ-Al$_2$O$_3$-honeycomb catalysts). As a result, the O_3 concentration over the Pd/γ-Al$_2$O$_3$-honeycomb catalysts is much lower in comparison with that of the γ-Al$_2$O$_3$-honeycomb catalysts and plasma alone. The presence of the catalyst further lowered the ozone concentration owing to the adsorption of ozone on the catalyst surface and subsequent dissociation into O atoms [13]. Particularly, the presence of the catalyst doped with Pd metal further enhanced the catalytic activity [45]. In addition, the O_3 concentration in the case of plasma alone suddenly increased in the initial stage and then decreased, which could be explained by the increase in the plasma reactor temperature [24]. The highlight is that the reaction temperature strongly affects O_3 decomposition [46].

Fig. 6(b) shows the FTIR spectra of the gaseous effluent after treatment by plasma only and by the plasma/catalyst combination consisting of the Pd/γ-Al$_2$O$_3$-honeycomb catalysts. Various emission peaks were detected in the case of plasma only, which reveals gas-phase byproducts.

In particular, the emission peak related to CO_2 is located at 2358 cm^{-1}. Other peaks including those of organic acid, acetone, alcohol, and aldehyde groups were also detected [2,47]. Interestingly, the CO_2 peak strongly intensifies in the case of the plasma/catalyst combination, whereas the other absorption peaks are minimized or disappear. This result indicates that the complete oxidation of EA over the plasma/catalyst was strongly improved. In addition, further information on the byproducts was obtained by conducting GC-MS analysis, resulting in the detection of organic byproducts such as ethanol (C$_2$H$_6$O), formic acid (HCOOH), acetone, acetic acid (CH$_3$COOH), and formaldehyde (HCHO) in the plasma only. In contrast, minor amounts of acetone were identified as a byproduct of the plasma catalytic process. Note that acetone is a stable compound that is hardly destroyed at low energy density [47,48].

3.3. Statistical analysis and the model fitting

A multivariate regression empirical formula between the removal efficiency, energy efficiency, and operating parameters was established. Three levels (-1, 0, and $+1$ coded for low, middle, and high values) of the three assigned variables were used for the analysis (Table 1). The

Table 3
ANOVA table for the response surface quadratic model.

Response	Model terms	Sum of square	Degree of freedom	Mean square	F-value	p-value (Prob. >F)	
Removal efficiency	Mode	4588.68	9	509.85	76.87	< 0.0001	significant
	X_1	3192.46	1	3192.46	481.35	< 0.0001	
	X_2	267.49	1	267.49	40.33	< 0.0001	
	X_3	690.01	1	690.01	104.04	< 0.0001	
	X_1X_2	70.97	1	70.97	10.7	0.0084	
	X_1X_3	83.25	1	83.25	12.55	0.0053	
	X_2X_3	30.55	1	30.55	4.61	0.0574	
	X_1^2	98.45	1	98.45	14.84	0.0032	
	X_2^2	0.103	1	0.103	0.0155	0.9033	
	X_3^2	6.34	1	6.34	0.9563	0.3512	
	Residual	66.32	10	6.63			
	Total	4655	19				
	$R^2 = 0.9858$, Adj. $R^2 = 0.9729$, Adequate precision = 34.4268, C.V. = 3.6%						
Energy efficiency	Mode	13.9	6	2.32	29.02	< 0.0001	significant
	X_1	3.43	1	3.43	42.92	< 0.0001	
	X_2	1.1	1	1.1	13.76	0.0026	
	X_3	7.75	1	7.75	97.06	< 0.0001	
	X_1X_2	0.8956	1	0.8956	11.22	0.0052	
	X_1X_3	0.0064	1	0.0064	0.0805	0.7811	
	X_2X_3	0.7228	1	0.7228	9.06	0.0101	
	Residual	1.04	13	0.0798			
	Total	14.93					

$R^2 = 0.9305$, Adj. $R^2 = 0.8985$, Adequate precision = 25.1365, C.V. = 11.52%.
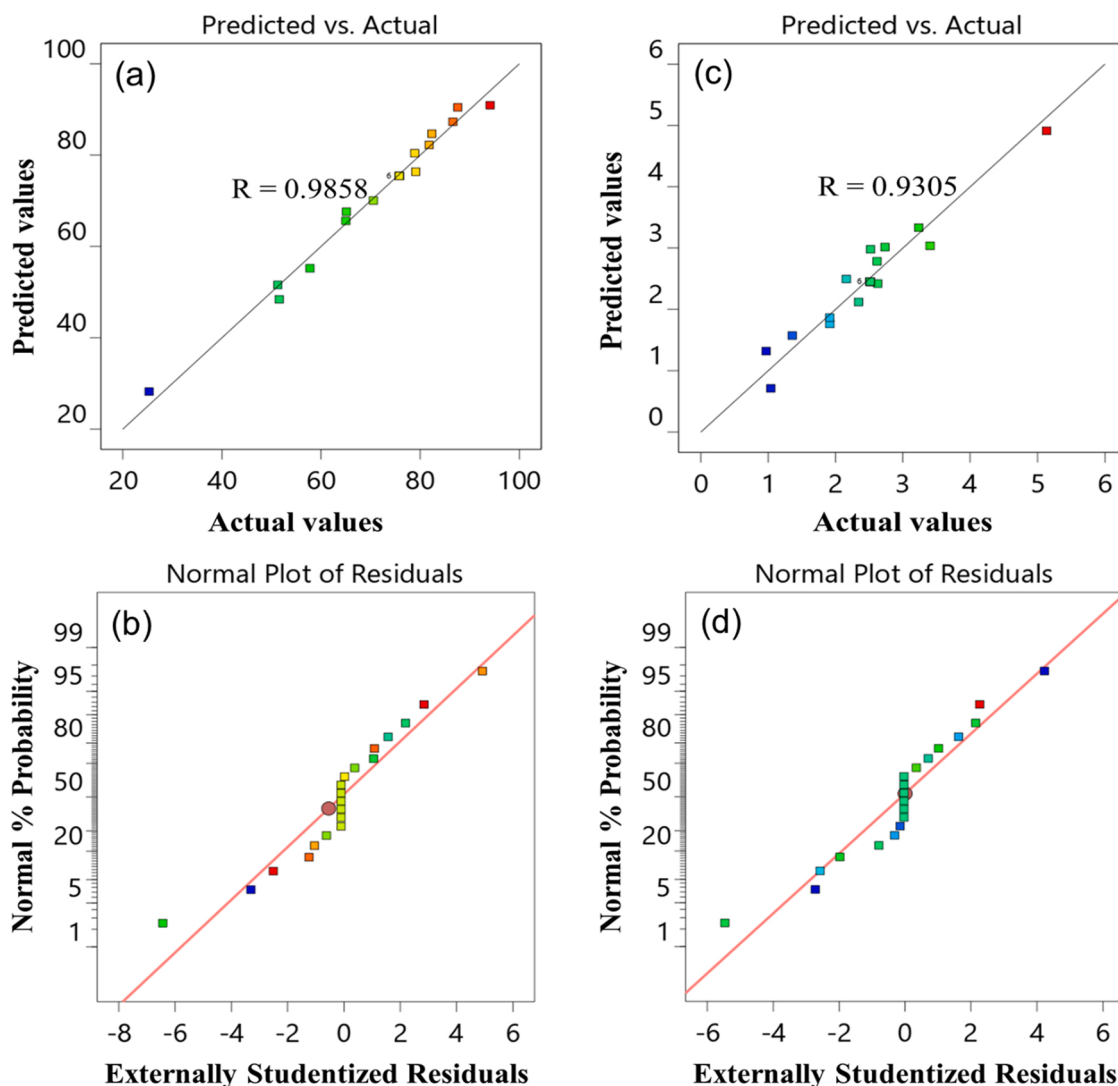
Fig. 7. The plot of predicted value versus actual values for (a-b) EA removal efficiency, (c-d) energy efficiency.

coefficients of the polynomial equation were computed from the experimental data according to CCD (Table 2) to analyze and predict the values of the response variables. Table 2 also presents the results regarding both the predicted and experimental values for removal efficiency, and clearly shows that the experimental values were in a good agreement with the predicted values. In addition, these experimental data were used to calculate the coefficient of the polynomial equation through analysis of variance (ANOVA). The regression equations for each response variable obtained from the RSM are given in Eqs. (10) and (11), respectively.

$$Y_1 = +75.44 + 17.48x_1 - 5.12x_2 - 8.06x_3 + 2.98x_1x_2 + 3.23x_1x_3 \\ - 1.95x_2x_3 - 5.98x_1^2 - 0.1935x_2^2 - 1.52x_3^2 \tag{10}$$

$$Y_2 = +2.45 - 0.5853x_1 - 0.3314x_2 + 0.8802x_3 + 0.3346x_1x_2 \\ - 0.00283x_1x_3 - 0.3006x_2x_3 \tag{11}$$

Statistical analysis (ANOVA) of the generated regression models for Eqs. (10) and (11) were performed to assess the suitability of the regression model. Table 3 presents the ANOVA results of the generated regression models. The data given in this table indicates that the experimental data can be well represented by the quadratic polynomial model; the coefficient of determination (R^2) values for the removal

efficiency (Y_1) and energy efficiency (Y_2) of the plasma catalytic EA removal are 0.9858 and 0.9305, respectively. These results suggested that at least 98.58% and 93.05% of the response values could be attributed to the identified independent variables. The P-values are less than the level of significance (< 0.05), which indicates that the model terms are significant relative to the pure error for all variables, which shows that our model is statistically accurate. Furthermore, the value of R^2 closer to unity and the model data fitting with the experimental results, indicated that the effect of variables on responses could be adequately described through a quadratic polynomial model [31]. A smaller P-value and a larger F-value are indicative of a significant effect of any term on the response variable [30,31]. Adequate precision (AP) is a signal-to-noise ratio of the models that shows the average prediction error; the AP values greater than 4 are desirable. In this work, the AP of 34.4268 for Y_1, and 25.1365 for Y_2 indicate the adequate intensity of the signals. AP values greater than 4 for all the responses indicate adequate model discrimination [31]. The reproducibility of the regression models was measured via the coefficients of variations (CV). The CV values are 3.6 for Y_1 and 11.52 for Y_2 (Table 3), indicating the reliability and reproducibility of the models. ANOVA statistical analysis of the data in Table 3 showed positive results for all the model responses. This can be seen in Fig. 7(a and c), which compares the actual measured values of removal efficiency and energy efficiency with the predicted responses plots from the model. The actual values were obtained by performing
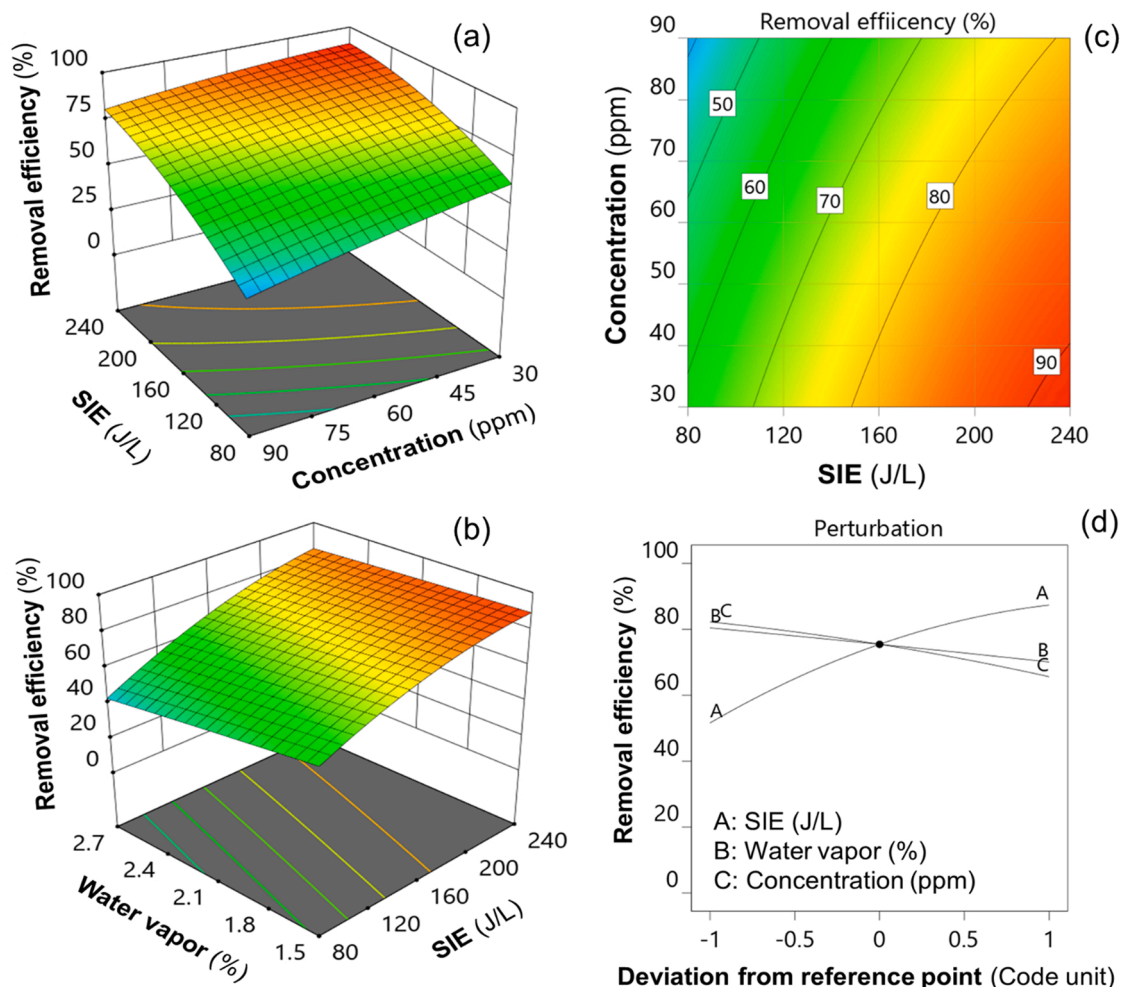
Fig. 8. Three-dimensional responses plot of the effect of independent variables (a) SIE and initial concentration, (b) SIE and water vapor, (c) contour plot for removal efficiency, and (d) the perturbation plot of the three factors on the plasma-catalytic EA removal efficiency at atmospheric pressure.

experiments for a particular run whereas the predicted values were calculated using Eqs. (10) and (11). The values in Fig. 7(a and c) revealed that the actual values were distributed relatively close to the straight line, indicating that the values predicted by the quadratic model equation were in good agreement with the responses from experimental results within an acceptable variance range. Fig. 7(b and d) illustrates the normal probability plots of the residuals and the plots of the residuals versus the predicted response variables (Y_1, and Y_2). The results reveal that the residuals generally lie on a straight line implying that the errors are normally distributed. To summarize, the obtained results suggest that the proposed models are suitable without any reason to suspect any violation of independence or constant variance assumption.

3.4. Effect of independent variables on response variables

The developed RSM-based mathematical model was conducted to calculate the interactive effect of independent variables at different levels such as the specific input energy (SIE), humidity, and initial concentration on the removal efficiency and energy efficiency. The results are presented in Table 2 and Figs. (8 and 9). As can be seen in the figures, the three-dimensional (3D) response surfaces based on a quadratic polynomial regression model provide new insights into the effects and relative importance of individual input parameters and their interactions on the plasma catalytic processing of ethyl acetate in terms of the EA removal efficiency and energy efficiency.

3.4.1. Removal efficiency

Fig. 8 presents the surface plot of the interactive effects of independent variables on the plasma-catalytic removal performance of EA. The influence of SIE and the initial concentration of EA on the removal efficiency is presented in Fig. 8(a). Both independent variables explicated the quadratic effect. As a result, the maximum EA removal efficiency based on the experimental data is 90.3% at the operating condition of 240 J/L, 2.1%, and 30 ppm. Increasing the initial concentration has a negative effect on the EA removal efficiency because more EA molecules are introduced into the reaction zone that requires further energy to decompose [4,25]. Indeed, increasing the initial concentration increases the number of EA molecules flowing into the reaction zone, whereas the amounts of reactive species, high-energy electrons, and active species generated by the plasma could be the same at a given SIE condition; therefore, the number of active species and electrons colliding with an EA molecule decrease. In addition, higher concentrations of EA in the gas stream may moderate the reaction between electrons and air, leading to a decrease in the formation of reactive species. Fig. 8(b) shows the interactive effect of SIE and water vapor on EA removal and energy efficiency. Notably, the EA removal efficiency increases significantly with an increase in the SIE due to more reactive chemical species generated in the reaction zone [14,26,49], which further promoted EA decomposition. In addition, the EA removal efficiency is only slightly lower with increasing water vapor in the gas stream. Higher water concentration in the gas stream can cover the surface of the catalyst and poison the catalyst by occupying active sites,
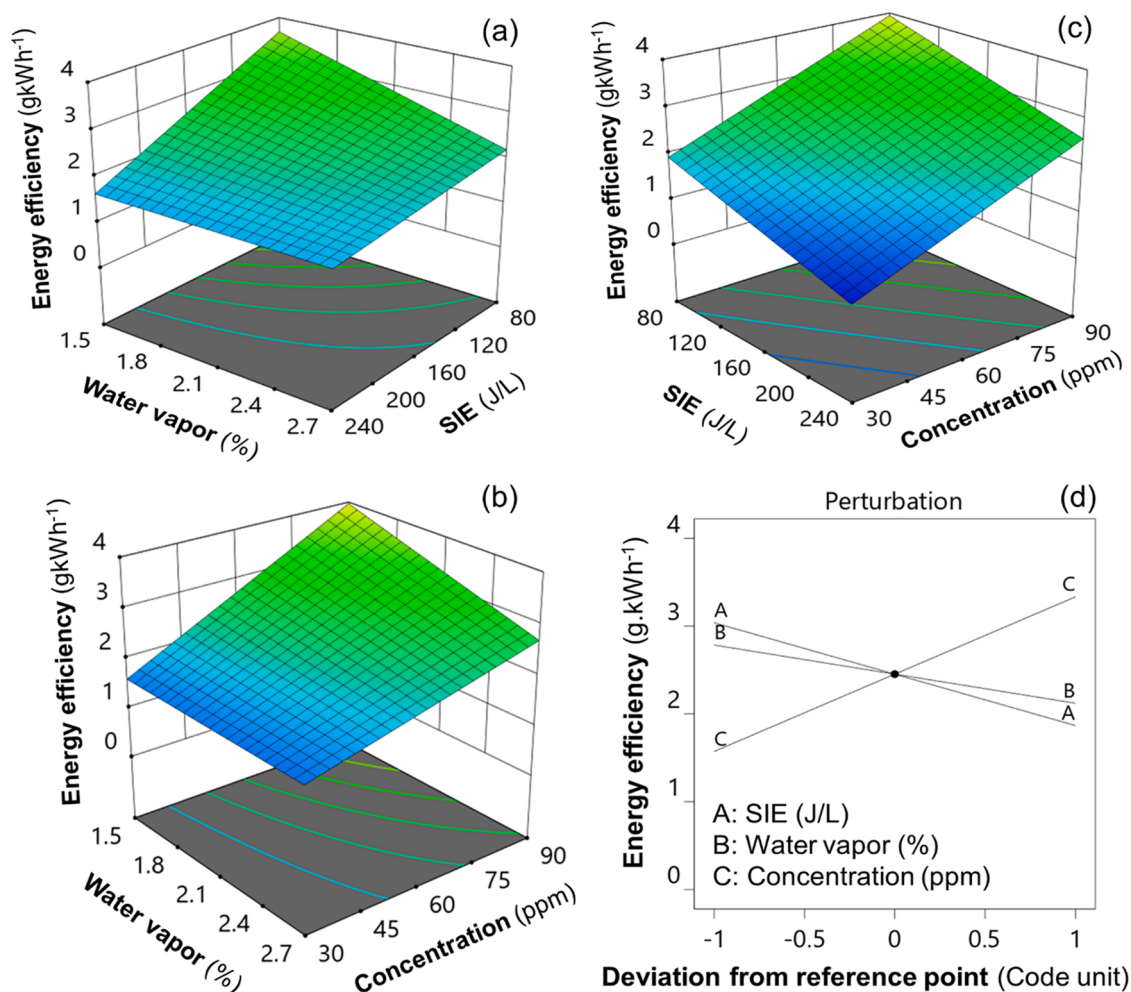
Fig. 9. Three-dimensional surface showing the effect of independent variables as (a) SIE and water vapor, (b) initial concentration and water vapor, (c) initial concentration and SIE, and (d) the perturbation plot of three factors on the energy efficiency of the plasma-catalytic reactor at atmospheric pressure.

resulting in a decrease in the number of active sites available for EA molecules because of the competitive adsorption of water molecules on active catalyst sites [50,51]. In addition, the increased water vapor may limit the electron density and quench the activated chemical species [26, 52]. Fig. 8(c) shows the contour plot as an estimate of the EA removal efficiency (in percent) as a function of two key parameters, SIE and the initial EA concentration. We found that the highest EA removal efficiency is achieved at the maximum SIE and the minimum EA concentration at the inlet. The regression curve of the sub-model shown in Fig. 8(d) indicates that the SIE and initial concentration have significant impacts on the EA removal efficiency whereas the effect of water vapor is less.

3.4.2. Energy efficiency

Fig. 9 shows the interaction effect of the input parameters on the energy efficiency (EE) of EA decomposition in the plasma catalytic reactor. Many factors have a significant effect on the EE including the

SIE, initial concentration, and water vapor. The interactive effect of SIE and water on EE is given in Fig. 9(a); both these variables have a linear effect. Higher EE corresponds to a decrease in SIE and water vapor content. A decrease in EE is observed with a lower initial concentration (Fig. 9(b and c)), although the removal efficiency shows the opposite trend, as mentioned above. The energy efficiency is inversely proportional to SIE and directly proportional to the initial concentration (Eq. 5). As the EA concentration increases from 30 to 90 ppm, EE increases from 1.99 to 3.97 g/kWh at SIE of 80 J/L, and water vapor of 2.1%. The effect of every single factor is indicated in Fig. 9(d). The initial concentration has a significant positive effect on EE; the value of EE increases strongly with an increase in the initial concentration.

3.5. Validation and verification of the predicted optimal conditions

Optimizing multiple independent variables to maximize the objective function is usually achieved through multiple sets of tests on a wide range of independent variables, which increases the cost in terms of time and labor. In this work, the respective values of EA removal in the plasma catalytic reactor were optimized by solving the regression equations based on RSM. If the partial derivative of Eq. (10) is zero, the three equations can be reconstructed as follows:

$$-11.96x_1 + 2.98x_2 + 3.23x_3 + 17.48 = 0 \tag{12}$$

$$2.98x_1 - 0.387 \ x_2 - 1.95x_3 - 5.12 = 0 \tag{13}$$

Table 4
Results of verification tests.

No.	SIE (J/L)	Water vapor (%)	Initial concentration (ppm)	Experimental value	Predict value
1	235	1.5	30.3	90.86	90.93
2	235	1.5	30.3	90.55	
3	235	1.5	30.3	91.06	

$$3.23x_1 - 1.95x_2 - 3.04x_3 - 8.05 = 0 \qquad (14)$$

The combination of Eqs. (6)–(8) and Eqs. (12)–(14) provides the parameters of the optimal conditions: $x_1 = 0.936$, $x_2 = -1.039$, $x_3 = -0.989$.

The set of optimal conditions above was selected to be validated experimentally and then these model equations were used to predict the value of the responses. The results are summarized in Table 4. As indicated by the data in Table 4, the empirical formula that expresses the performance of the plasma catalytic reactor for EA removal, and that was established using experimental design and regression analysis, has higher credibility. The experimental values were found to be in good agreement with the values predicted by the model (Fig. 7 and Table 2), demonstrating the precision and reliability of the empirical models. Briefly, the proposed regression models are satisfactory and accurate.

4. Conclusions

The high throughput removal of EA in a plasma catalytic reactor over a practical-scale $Pd/\gamma-Al_2O_3$/honeycomb catalyst was investigated. A uniform corona discharge was created inside the entire chamber of the $Pd_{0.02}/\gamma-Al_2O_3$/honeycomb catalyst, which is the key to have high EA removal efficiency. Furthermore, the results of the SEM, XRD, and XPS analyses revealed that the properties of the coated $Pd/\gamma-Al_2O_3$ catalyst layer on the monolith strongly enhanced the oxidation of EA in the plasma-catalytic reactor. This work launched a highly effective technology for high throughput EA removal on an industrial scale.

In addition, this work produced a combined desirability value for all the factors and responses via a mathematic model based on RSM. ANOVA analysis yielded a high coefficient of determination values ($R_1^2 = 0.9858$, and $R_2^2 = 0.9305$). The analysis results indicated that the SIE was the most significant factor affecting the removal efficiency of EA, whilst the water vapor and initial concentration have the least influence on the performance of the plasma-catalytic process. Systematic analysis with the model enabled the optimal conditions to be derived with EA removal efficiency of 90.93% and 2.91 g kWh^{-1} of energy efficiency at 235 J/L SIE, 1.5% water vapor, and 30.3 ppm EA at the inlet. The good agreement between the predicted values and the experimental data indicates that the RSM model is an effective approach to predict the practical removal of VOCs using the plasma catalysts system. This study introduced a valuable approach for fast and reliable simulation and prediction of the complex plasma catalytic process.

CRediT authorship contribution statement

Van Toan Nguyen: Conceptualization, Methodology, Investigation, Visualization, Data analysis, Writing – original draft. **Duy Khoe Dinh:** Data analysis, Validation, Writing – review & editing. **Young Sun Mok:** Supervision, Writing – review & editing, Funding acquisition, Resources. **Kyeong Hwan Yoon:** Data analysis, Validation. **Van Duong Dao:** Data analysis, Validation. **Shirjana Saud:** Data analysis, Validation. **Mokter Hossain:** Data analysis, Validation. **Teke Sosiawati:** Data analysis, Validation.

Declaration of Competing Interest

The authors declare that they have no known competing financial interests or personal relationships that could have appeared to influence the work reported in this paper.

Acknowledgments

References

[1] X. Zhu, S. Zhang, Y. Yang, C. Zheng, J. Zhou, X. Gao, X. Tu, Enhanced performance for plasma-catalytic oxidation of ethyl acetate over La1-xCexCoO3+Δ catalysts, Appl. Catal. B Environ. 213 (2017) 97–105, https://doi.org/10.1016/j.apcatb.2017.04.066.

[2] H. Wang, S. Chen, Z. Wang, Y. Zhou, Z. Wu, A novel hybrid Bi2MoO6-MnO2 catalysts with the superior plasma induced pseudo photocatalytic-catalytic performance for ethyl acetate degradation, Appl. Catal. B Environ. 254 (2019) 339–350, https://doi.org/10.1016/j.apcatb.2019.05.018.

[3] Q. Dai, H. Huang, Y. Zhu, W. Deng, S. Bai, X. Wang, G. Lu, Catalysis oxidation of 1,2-dichloroethane and ethyl acetate over ceria nanocrystals with well-defined crystal planes, Appl. Catal. B Environ. 117–118 (2012) 360–368, https://doi.org/10.1016/j.apcatb.2012.02.001.

[4] V.T. Nguyen, D.B. Nguyen, Y.S. Mok, M.M. Hossain, S. Saud, K.H. Yoon, D.K. Dinh, S. Ryu, H. Jeon, S.B. Kim, Removal of ethyl acetate in air by using different types of corona discharges generated in a honeycomb monolith structure coated with Pd/γ-alumina, J. Hazard. Mater. 416 (2021), 126162, https://doi.org/10.1016/j.jhazmat.2021.126162.

[5] J. Lyu, J. Gao, M. Zhang, Q. Fu, L. Sun, S. Hu, J. Zhong, S. Wang, J. Li, Construction of homojunction-adsorption layer on anatase TiO2 to improve photocatalytic mineralization of volatile organic compounds, Appl. Catal. B Environ. 202 (2017) 664–670, https://doi.org/10.1016/j.apcatb.2016.09.041.

[6] P. Li, S. Kim, J. Jin, H.C. Do, J.H. Park, Efficient photodegradation of volatile organic compounds by iron-based metal-organic frameworks with high adsorption capacity, Appl. Catal. B Environ. 263 (2020) 1–9, https://doi.org/10.1016/j.apcatb.2019.118284.

[7] Z. Qu, Y. Bu, Y. Qin, Y. Wang, Q. Fu, The effects of alkali metal on structure of manganese oxide supported on SBA-15 for application in the toluene catalytic oxidation, Chem. Eng. J. 209 (2012) 163–169, https://doi.org/10.1016/j.cej.2012.07.138.

[8] D.M. Gómez, J.M. Gatica, J.C. Hernández-Garrido, G.A. Cifredo, M. Montes, O. Sanz, J.M. Rebled, H. Vidal, A novel CoOx/La-modified-CeO2 formulation for powdered and washcoated onto cordierite honeycomb catalysts with application in VOCs oxidation, Appl. Catal. B Environ. 144 (2014) 425–434, https://doi.org/10.1016/j.apcatb.2013.07.045.

[9] Y. Guo, M. Wen, G. Li, T. An, Recent advances in VOC elimination by catalytic oxidation technology onto various nanoparticles catalysts: a critical review, Appl. Catal. B Environ. 281 (2021), 119447, https://doi.org/10.1016/j.apcatb.2020.119447.

[10] X. Wang, X. Jia, J. Wen, Transient modeling of toluene waste gas biotreatment in a gas-liquid airlift loop reactor, Chem. Eng. J. 159 (2010) 1–10, https://doi.org/10.1016/j.cej.2010.02.006.

[11] J. Van Durme, J. Dewulf, C. Leys, H. Van Langenhove, Combining non-thermal plasma with heterogeneous catalysis in waste gas treatment: a review, Appl. Catal. B Environ. 78 (2008) 324–333, https://doi.org/10.1016/j.apcatb.2007.09.035.

[12] K. Barbusinski, K. Kalemba, D. Kasperczyk, K. Urbaniec, V. Kozik, Biological methods for odor treatment – a review, J. Clean. Prod. 152 (2017) 223–241, https://doi.org/10.1016/j.jclepro.2017.03.093.

[13] A.M. Harling, D.J. Glover, J.C. Whitehead, K. Zhang, The role of ozone in the plasma-catalytic destruction of environmental pollutants, Appl. Catal. B Environ. 90 (2009) 157–161, https://doi.org/10.1016/j.apcatb.2009.03.005.

[14] X. Fan, T. Zhu, Y. Sun, X. Yan, The roles of various plasma species in the plasma and plasma-catalytic removal of low-concentration formaldehyde in air, J. Hazard. Mater. 196 (2011) 380–385, https://doi.org/10.1016/j.jhazmat.2011.09.044.

[15] X. Zhu, X. Gao, R. Qin, Y. Zeng, R. Qu, C. Zheng, X. Tu, Plasma-catalytic removal of formaldehyde over Cu-Ce catalysts in a dielectric barrier discharge reactor, Appl. Catal. B Environ. 170–171 (2015) 293–300, https://doi.org/10.1016/j.apcatb.2015.01.032.

[16] X. Zhu, X. Gao, R. Qin, Y. Zeng, R. Qu, C. Zheng, X. Tu, Plasma-catalytic removal of formaldehyde over Cu-Ce catalysts in a dielectric barrier discharge reactor, Appl. Catal. B Environ. 170–171 (2015) 293–300, https://doi.org/10.1016/j.apcatb.2015.01.032.

[17] C. Norsic, J.M. Tatibouët, C. Batiot-Dupeyrat, E. Fourré, Non thermal plasma assisted catalysis of methanol oxidation on Mn, Ce and Cu oxides supported on γ-Al2O3, Chem. Eng. J. 304 (2016) 563–572, https://doi.org/10.1016/j.cej.2016.06.091.

[18] M. Magureanu, N.B. Mandache, P. Eloy, E.M. Gaigneaux, V.I. Parvulescu, Plasma-assisted catalysis for volatile organic compounds abatement, Appl. Catal. B Environ. 61 (2005) 12–20, https://doi.org/10.1016/j.apcatb.2005.04.007.

[19] J. Jarrige, P. Vervisch, Plasma-enhanced catalysis of propane and isopropyl alcohol at ambient temperature on a MnO2-based catalyst, Appl. Catal. B Environ. 90 (2009) 74–82, https://doi.org/10.1016/j.apcatb.2009.02.015.

[20] Y.R. Zhang, K. Van Laer, E.C. Neyts, A. Bogaerts, Can plasma be formed in catalyst pores? A modeling investigation, Appl. Catal. B Environ. 185 (2016) 56–67, https://doi.org/10.1016/j.apcatb.2015.12.009.

[21] H. Zhang, K. Li, T. Sun, J. Jia, Z. Lou, L. Feng, Removal of styrene using dielectric barrier discharge plasmas combined with sol-gel prepared TiO2 combined γ-Al2O3, Chem. Eng. J. 241 (2014) 92–102, https://doi.org/10.1016/j.cej.2013.12.019.

[22] X. Zhu, S. Liu, Y. Cai, X. Gao, J. Zhou, C. Zheng, X. Tu, Post-plasma catalytic removal of methanol over Mn-Ce catalysts in an atmospheric dielectric barrier discharge, Appl. Catal. B Environ. 183 (2016) 124–132, https://doi.org/10.1016/j.apcatb.2015.10.013.

[23] Y. Wan, X. Fan, T. Zhu, Removal of low-concentration formaldehyde in air by DC corona discharge plasma, Chem. Eng. J. 171 (2011) 314–319, https://doi.org/10.1016/j.cej.2011.04.011.

[24] V.T. Nguyen, D.B. Nguyen, I. Heo, Y.S. Mok, Efficient degradation of styrene in a nonthermal plasma–catalytic system over Pd/ZSM-5 catalyst, Plasma Chem. Plasma Process. 40 (2020) 1207–1220, https://doi.org/10.1007/s11090-020-10088-w.

[25] S. Li, X. Dang, X. Yu, G. Abbas, Q. Zhang, L. Cao, The application of dielectric barrier discharge non-thermal plasma in VOCs abatement: a review, Chem. Eng. J. 388 (2020), 124275, https://doi.org/10.1016/j.cej.2020.124275.

[26] V. Toan Nguyen, K. Hwan Yoon, Y. Sun Mok, D. Ba Nguyen, D. Khoe Dinh, M. Mokter Hossain, S. Saud, S.-J. Kim, Y. Jin Kim, J. Hee Lee, I. Heo, Practical-scale honeycomb catalytic reactor coupled with non-thermal plasma for high-throughput removal of isopropanol, Chem. Eng. J. 430 (2021), 132905, https://doi.org/10.1016/j.cej.2021.132905.

[27] W.S. Kang, D.H. Lee, J.O. Lee, M. Hur, Y.H. Song, Combination of plasma with a honeycomb-structured catalyst for automobile exhaust treatment, Environ. Sci. Technol. 47 (2013) 11358–11362, https://doi.org/10.1021/es402477a.

[28] S. Hosseini, H. Moghaddas, S. Masoudi Soltani, S. Kheawhom, Technological applications of honeycomb monoliths in environmental processes: a review, Process Saf. Environ. Prot. 133 (2020) 286–300, https://doi.org/10.1016/j.psep.2019.11.020.

[29] P. Avila, M. Montes, E.E. Miró, Monolithic reactors for environmental applications: a review on preparation technologies, Chem. Eng. J. 109 (2005) 11–36, https://doi.org/10.1016/j.cej.2005.02.025.

[30] D. Vildozo, C. Ferronato, M. Sleiman, J.M. Chovelon, Photocatalytic treatment of indoor air: optimization of 2-propanol removal using a response surface methodology (RSM), Appl. Catal. B Environ. 94 (2010) 303–310, https://doi.org/10.1016/j.apcatb.2009.11.020.

[31] S. Ghafari, H.A. Aziz, M.H. Isa, A.A. Zinatizadeh, Application of response surface methodology (RSM) to optimize coagulation-flocculation treatment of leachate using poly-aluminum chloride (PAC) and alum, J. Hazard. Mater. 163 (2009) 650–656, https://doi.org/10.1016/j.jhazmat.2008.07.090.

[32] C. Xu, W. Sun, L. Cao, T. Li, X. Cai, J. Yang, Highly efficient Pd-doped aluminate spinel catalysts with different divalent cations for the selective catalytic reduction of NO with H2 at low temperature, Chem. Eng. J. 308 (2017) 980–987, https://doi.org/10.1016/j.cej.2016.09.119.

[33] M.J. Hazlett, M. Moses-Debusk, J.E. Parks, L.F. Allard, W.S. Epling, Kinetic and mechanistic study of bimetallic Pt-Pd/Al2O3 catalysts for CO and C3H6 oxidation, Appl. Catal. B Environ. 202 (2017) 404–417, https://doi.org/10.1016/j.apcatb.2016.09.034.

[34] D.W. Lee, M.H. Jin, Y.J. Lee, J.H. Park, C.B. Lee, J.S. Park, Reducing-agent-free instant synthesis of carbon-supported Pd catalysts in a Green Leidenfrost Droplet Reactor and catalytic activity in formic acid dehydrogenation, Sci. Rep. 6 (2016) 1–9, https://doi.org/10.1038/srep26474.

[35] S.J. Park, I. Bae, I.S. Nam, B.K. Cho, S.M. Jung, J.H. Lee, Oxidation of formaldehyde over Pd/Beta catalyst, Chem. Eng. J. 195–196 (2012) 392–402, https://doi.org/10.1016/j.cej.2012.04.028.

[36] Y. Wang, C. Zhang, F. Liu, H. He, Well-dispersed palladium supported on ordered mesoporous Co3O4 for catalytic oxidation of o-xylene, Appl. Catal. B Environ. 142–143 (2013) 72–79, https://doi.org/10.1016/j.apcatb.2013.05.003.

[37] L.M.T. Simplício, S.T. Brandão, E.A. Sales, L. Lietti, F. Bozon-Verduraz, Methane combustion over PdO-alumina catalysts: the effect of palladium precursors, Appl. Catal. B Environ. 63 (2006) 9–14, https://doi.org/10.1016/j.apcatb.2005.08.009.

[38] H. He, X. Lin, S. Li, Z. Wu, J. Gao, J. Wu, W. Wen, D. Ye, M. Fu, The key surface species and oxygen vacancies in MnOx(0.4)-CeO2 toward repeated soot oxidation,

[39] X. Zhu, X. Tu, M. Chen, Y. Yang, C. Zheng, J. Zhou, X. Gao, La0.8M0.2MnO3 (M = Ba, Ca, Ce, Mg and Sr) perovskite catalysts for plasma-catalytic oxidation of ethyl acetate, Catal. Commun. 92 (2017) 35–39, https://doi.org/10.1016/j.catcom.2016.12.013.

[40] V.P. Santos, M.F.R. Pereira, J.J.M. Órfão, J.L. Figueiredo, The role of lattice oxygen on the activity of manganese oxides towards the oxidation of volatile organic compounds, Appl. Catal. B Environ. 99 (2010) 353–363, https://doi.org/10.1016/j.apcatb.2010.07.007.

[41] Y. Huang, Y. Liu, W. Wang, M. Chen, H. Li, S. Cheng Lee, W. Ho, T. Huang, J. Cao, Oxygen vacancy–engineered δ-MnOx/activated carbon for room-temperature catalytic oxidation of formaldehyde, Appl. Catal. B Environ. 278 (2020), 119294, https://doi.org/10.1016/j.apcatb.2020.119294.

[42] N. Jiang, Y. Zhao, C. Qiu, K. Shang, N. Lu, J. Li, Y. Wu, Y. Zhang, Enhanced catalytic performance of CoOx-CeO2 for synergetic degradation of toluene in multistage sliding plasma system through response surface methodology (RSM), Appl. Catal. B Environ. 259 (2019), https://doi.org/10.1016/j.apcatb.2019.118061.

[43] H.H. Kim, A. Ogata, S. Futamura, Oxygen partial pressure-dependent behavior of various catalysts for the total oxidation of VOCs using cycled system of adsorption and oxygen plasma, Appl. Catal. B Environ. 79 (2008) 356–367, https://doi.org/10.1016/j.apcatb.2007.10.038.

[44] Y.S. Mok, Absorption-reduction technique assisted by ozone injection and sodium sulfide for NOx removal from exhaust gas, Chem. Eng. J. 118 (2006) 63–67, https://doi.org/10.1016/j.cej.2006.01.011.

[45] F. Bi, X. Zhang, J. Chen, Y. Yang, Y. Wang, Excellent catalytic activity and water resistance of UiO-66-supported highly dispersed Pd nanoparticles for toluene catalytic oxidation, Appl. Catal. B Environ. 269 (2020), 118767, https://doi.org/10.1016/j.apcatb.2020.118767.

[46] J. Jia, P. Zhang, L. Chen, Catalytic decomposition of gaseous ozone over manganese dioxides with different crystal structures, Appl. Catal. B Environ. 189 (2016) 210–218, https://doi.org/10.1016/j.apcatb.2016.02.055.

[47] H.Q. Trinh, Y.S. Mok, Plasma-catalytic oxidation of acetone in annular porous monolithic ceramic-supported catalysts, Chem. Eng. J. 251 (2014) 199–206, https://doi.org/10.1016/j.cej.2014.04.071.

[48] C. Barakat, P. Gravejat, O. Guaitella, F. Thevenet, A. Rousseau, Oxidation of isopropanol and acetone adsorbed on TiO2 under plasma generated ozone flow: gas phase and adsorbed species monitoring, Appl. Catal. B Environ. 147 (2014) 302–313, https://doi.org/10.1016/j.apcatb.2013.09.008.

[49] J. Wu, Q. Xia, H. Wang, Z. Li, Catalytic performance of plasma catalysis system with nickel oxide catalysts on different supports for toluene removal: effect of water vapor, Appl. Catal. B Environ. 156–157 (2014) 265–272, https://doi.org/10.1016/j.apcatb.2014.03.017.

[50] T.T. Yang, H.T. Bi, X. Cheng, Effects of O2, CO2 and H2O on NOx adsorption and selective catalytic reduction over Fe/ZSM-5, Appl. Catal. B Environ. 102 (2011) 163–171, https://doi.org/10.1016/j.apcatb.2010.11.038.

[51] J. Van Durme, J. Dewulf, K. Demeestere, C. Leys, H. Van Langenhove, Post-plasma catalytic technology for the removal of toluene from indoor air: effect of humidity, Appl. Catal. B Environ. 87 (2009) 78–83, https://doi.org/10.1016/j.apcatb.2008.08.015.

[52] F. Thevenet, O. Guaitella, E. Puzenat, C. Guillard, A. Rousseau, Influence of water vapor on plasma/photocatalytic oxidation efficiency of acetylene, Appl. Catal. B Environ. 84 (2008) 813–820, https://doi.org/10.1016/j.apcatb.2008.06.029.

Appl. Catal. B Environ. 223 (2018) 134–142, https://doi.org/10.1016/j.apcatb.2017.08.084.